PCCP

ROYAL SOCIETY OF CHEMISTRY

PAPER

View Article Online
View Journal

Cite this: DOI: 10.1039/d6cp00517a

Internal rotation-induced *A*/*E* splittings in the methyl rocking band of propylene oxide (ν_{17} = 1) and refined analyses of the ground and first torsional states (ν_{24} = 1)

Karel Vávra,[ab] Kateřina Luková,[ab] Eileen Döring,[a] Jan Jakob,[a] Thomas F. Giesen *[a] and Guido W. Fuchs[a]

Received 11th February 2026,
Accepted 8th April 2026

DOI: 10.1039/d6cp00517a

rsc.li/pccp

The ro-vibrational spectrum of propylene oxide in the methyl rocking fundamental band ν_{17} = 1 is reported for the first time, based on high-resolution infrared measurements at room temperature and under supersonic jet-cooled conditions. The band origin and symmetry-resolved molecular parameters were determined with high precision. Unexpectedly large splittings into *A*- and *E*-symmetry components are observed in the jet-cooled spectrum, indicating perturbative coupling of the ν_{17} state with nearby torsionally excited dark states. The spectra were analysed using an effective Hamiltonian approach implemented in the newly developed General Fitting Code (GFC), which enables a consistent treatment of rovibrational and torsional interactions. In addition, previously published microwave, millimetre- and submillimetre-wave spectra of the ground torsional state and the first torsionally excited state ν_{24} = 1 were reanalysed using refined data sets. A simultaneous treatment of both torsional states allows an independent determination of the internal rotation constant F_0 and the threefold torsional barrier height V_3, as well as improved values for higher-order barrier terms.

1 Introduction

Propylene oxide (CH_3CHCH_2O, see Fig. 1A), also known as methyl oxirane, is a stable chiral molecule that has been widely investigated using various spectroscopic techniques (see ref. 1 and references therein) and quantum chemical calculations.[2–5] It has also been detected in space through radio astronomical observations, and is the first chiral interstellar molecule to be found so far.[6] Because of its conformational stability and the commercial availability of enantiomerically pure samples, propylene oxide (PO) is frequently used in studies of molecular chirality. In addition, the methyl group in PO acts as an internal rotor, giving rise to a torsional motion which leaves a spectral fingerprint in high-resolution spectra. This torsional motion has been the subject of intensive research for several decades and is also an important aspect of this work due to the potential for anharmonic couplings between the fundamental vibration ν_{17} and highly excited torsional motions.

The study of the effects of internal rotation in PO began in 1957, when Swalen *et al.* analysed the ground and first excited torsional states.[7] They reported barrier heights of V_3^0 = 974 cm^{-1} and V_3^1 = 895 cm^{-1}, respectively. In a subsequent study,[8] the same group extended their analysis to higher rotational quantum numbers (J, K) and included the second torsional state, determining a consistent barrier height of $V_3^{0,1,2}$ = 895 (25) cm^{-1}. They concluded that the coupling between internal rotation and molecular vibrations was negligible and that the V_6 term was both insignificant and indeterminable.

Subsequent far-infrared measurements[9] and direct observations of transitions between torsionally excited states refined the barrier height to V_3 = 900 (8) cm^{-1} and V_6 = −9 (1) cm^{-1}. More recently, Mesko *et al.*[10] analysed the spectrum of the ground torsional state in the millimetre and submillimetre region (70 GHz–1 THz), determining V_3^0 = 892.71 (58) cm^{-1}. Stahl *et al.*[11] investigated the first torsional state in the 75–950 GHz range and obtained V_3^1 = 898.661 (89) cm^{-1}. Although internal rotation effects were also observed in the CH_3 stretching region (2500–3100 cm^{-1}),[12] *i.e.*, in vibrationally excited high-lying states, attempts to derive barrier heights from this region were unsuccessful.

Studies of vibrationally excited states have been performed by Ainetschian *et al.*[13] for propene (propylene), *i.e.* a molecule similar to propylene oxide that also contains a methyl group. The region of 900–1100 cm^{-1} was measured and it was found that the *A*/*E* splitting due to internal methyl rotation varied

[a] Institute of Physics, University of Kassel, Heinrich-Plett-Str. 40, 34132 Kassel, Germany. E-mail: t.giesen@uni-kassel.de
[b] Department of Analytical Chemistry, University of Chemistry and Technology, Technická 5, 166 28 Prague 6, Czech Republic

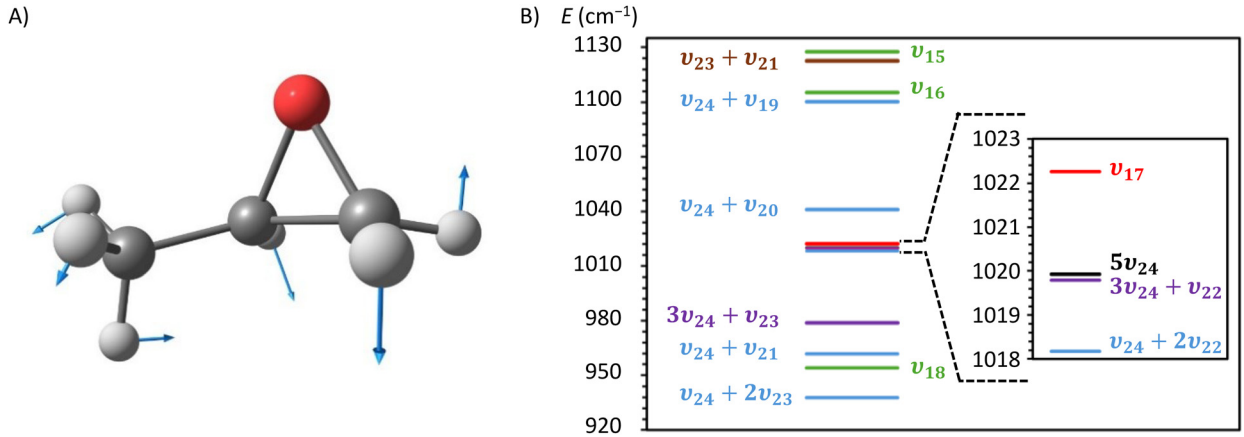

Fig. 1 (A) Visualization of the ν_{17} = 1 vibrational mode of propylene oxide. The blue arrows show the normal coordinate displacement vectors. (B) Predicted anharmonic vibrational energies of modes (MP2/cc-aug-pVTZ) in the proximity of ν_{17} = 1. The energies of the combination modes were derived as linear combinations of the energies of the corresponding fundamental modes. Combination modes that do not involve torsional modes have been omitted for clarity. Also, the internal rotation splitting is not considered for torsionally excited states. All energies are given relative to the ground vibrational state.

significantly between the ground state and different vibrational states. These discrepancies were attributed to anharmonic coupling between fundamental vibrations and torsional overtones or combination bands. Lafferty *et al.*[14] later confirmed this unusual behaviour using jet-cooled molecular spectroscopy in the 930–1030 cm^{-1} region. They concluded that barrier heights derived solely from line splittings in vibrationally excited states are unreliable and that a more comprehensive analysis is required. Nevertheless, unlike the well-characterized internal rotation effects observed in the ground and torsional states, the behaviour of internal rotors in vibrationally excited states remains largely unexplored for propylene oxide and many other molecules. The limited number of studies on this subject highlights its complexity and the need for more systematic research. Getting a deeper insight into molecular dynamics requires an understanding of the coupling between internal rotation (a large-amplitude motion) and methyl rocking vibrations (small-amplitude motions). Thus, this work can be considered a case study that helps understanding the spectroscopic behaviour of similar molecules and possibly also the phenomena of intramolecular vibrational energy redistribution (IVR).

This study presents the first successful simultaneous analysis of torsional *A*/*E* splitting in both the ground and vibrationally excited states of propylene oxide. We used high-resolution infrared spectroscopy and advanced computational modelling to study the fundamental vibrational band ν_{17} = 1 of PO. Furthermore, we analysed the ground and first torsional states of PO using experimental data from ref. 10, 11 thereby providing a unified framework for interpreting internal rotation in both the ground and excited vibrational states. The infrared band ν_{17} was recorded in a glass cell at room temperature at frequencies ranging from 1006.6 to 1033.7 cm^{-1} and under supersonic expansion conditions ranging from 1009.8 to 1032.8 cm^{-1}. From the observed and assigned transitions, we determined the ν_{17} band origin, the rotational and quartic centrifugal distortion constants, and the effective potential barrier height. The analysis was performed using the newly developed General Fitting Code (GFC), which enabled us to treat internal rotation effects consistently across multiple vibrational states.

2 Experimental details

A high-resolution infrared spectroscopic study was performed using a racemic mixture of propylene oxide (CAS 75-56-9), which was purchased from Sigma Aldrich and had a purity of over 99.5%. The infrared absorption spectra were recorded using two experimental setups: one with a glass cell at room temperature under static pressure conditions, and the other with a pick-up source in combination with a supersonic jet expansion under vacuum conditions.

An external cavity quantum cascade laser (ec-QCL; Daylight Solutions) with a laser power of 100 mW, operating in the range of 990 to 1060 cm^{-1} (9.4 to 10.1 μm) was used to record the spectrum. For the room temperature spectrum the laser frequency was slowly tuned over the spectral range, while for the supersonic jet measurements a fast scanning current modulation mode was used to record narrow spectral segments of 0.03 cm^{-1} width. Each segment was measured 600 times, averaged and combined to create a complete broadband spectrum.

To calibrate the wavelength of the recorded spectra, a small fraction (5–10%) of the infrared radiation was used to record the transmission simultaneously of both an etalon with a free spectral range (FSR) of 150 MHz and a methanol (CH_3OH) reference gas spectrum. Room-temperature spectra were acquired using an 80 cm long glass absorption cell filled with propylene oxide vapor at a pressure of 3 mbar. The transmitted light intensity was detected using a liquid nitrogen-cooled mercury cadmium telluride detector (lq-N_2 MCT Teledyne Judson Technology).

The supersonic jet spectrum was recorded at around 35 Kelvin, with significantly reduced line widths of approximately 40 MHz (FWHM) compared to the room temperature measurement of approximately 120 MHz (FWHM). The uncertainties of the measured line positions were estimated from the calibration procedure, the reproducibility of repeated scans, and the observed linewidths. Based on the etalon calibration and the methanol reference spectrum, individual uncertainties were assigned to each transition frequency. Typical uncertainties correspond to about 4×10^{-3} cm^{-1} ($\approx$120 MHz) for room-temperature spectra and about 1.33×10^{-3} cm^{-1} ($\approx$40 MHz) for the jet-cooled spectra. Larger uncertainties (up to 2×10^{-2} cm^{-1}) were used for weak or partially blended transitions. These uncertainties are reflected in the RMS values of the fits and are listed line-by-line in the tables of assigned transitions. Rotational quantum numbers up to $J = 17$ were observed. A pick-up source filled with liquid propylene oxide was used for the measurements. The evaporating sample was diluted in 5 bar of helium gas, pre-expanded through a pulsed valve into a slit nozzle source, and then adiabatically expanding into a vacuum chamber at a background pressure of 10^{-2} mbar.

The infrared laser beam intersected the supersonic jet perpendicularly, 10 mm downstream from the slit nozzle exit, 42 times in a Herriott-type multi-pass configuration to enhance the absorption signal. The signal was recorded by a fast liquid-N_2 cooled MCT detector (Vigo Photonics). The current modulation of the ec-QCL used, approximately 200 kHz, was fast enough to resolve the transit time of 10 μs of the jet molecules passing through the laser beam.[15]

2.1 Software

The General Fitting Code (GFC), a new fitting program, was used to process the measured spectra and calculate and visualize the spectral predictions. The program was also used to fit the transitions of the vibrationally excited state of propylene oxide $\nu_{17} = 1$. The assignments of the transitions of the $\nu_{17} = 1$ mode were aided by Loomis-Wood type plots. Additionally, previously published data for the ground and first torsionally excited states[10,11] were re-analyzed using GFC. Internal rotation tunneling splitting was treated within the framework of the Combined Axis Method (CAM)[16] employing Watson's effective rotational Hamiltonian in the *A*-reduction and I^r representation.[17] Further details on the program's functionality and the methods employed are provided in Appendix A.

3 Theory

The analysis of molecules containing methyl internal rotors has been addressed by several effective Hamiltonian approaches and corresponding fitting programs. Comprehensive overviews of the available methods and codes for asymmetric top molecules with a single C_{3v} internal rotor have been given, for example, by Kleiner.[18] Two of the most widely used approaches are implementations based on the combined axis method (CAM) and the rho-axis method (RAM). CAM-type formulations treat the torsion–rotation interaction in a coordinate system related to the principal inertial axes and are implemented in programs such as XIAM,[19] which has been applied successfully to many molecules with methyl internal rotation. RAM-based approaches, implemented for example in the BELGI program family,[20] use a coordinate system aligned with the internal rotor axis and allow a global treatment of torsion–rotation interactions involving several torsional states. These methods are routinely applied not only to rotational spectra but also to rovibrational spectra. For example, recent microwave and quantum cascade laser infrared studies of isoprene have used both XIAM and BELGI to analyse torsion–rotation interactions and unusually large *A*/*E* splittings arising from coupling with nearby torsionally excited states.[21]

In addition, several other programs provide alternative strategies for analysing torsion–rotation interactions. ERHAM[22,23] expands torsional splittings and rotational constants as Fourier series in the internal rotation angle, treating each torsional state independently. RAM36[24] extends the rho-axis method to molecules with three- and sixfold barriers and enables a global simultaneous fit of multiple torsional states. More recently, Westerfit[25] has been developed for open-shell molecules, incorporating spin–torsion–rotation interactions within the RAM framework.

Against this background, the present work follows a related approach: the torsion–rotation interaction is treated within a Hamiltonian framework closely related to the combined axis method, implemented in the newly developed General Fitting Code (GFC). The code provides a flexible environment for the simultaneous treatment of rotational and rovibrational data of molecules containing a single methyl internal rotor, extending the CAM approach to a global treatment of multiple torsional and vibrational states. The rotational–torsional–vibrational structure of propylene oxide is described using an effective Hamiltonian approach. The total Hamiltonian operator is written as

$$\boldsymbol{H}_{\mathrm{tot}} = \boldsymbol{H}_{\mathrm{v}} + \boldsymbol{H}_{\mathrm{R}} + \boldsymbol{H}_{\mathrm{T}} + \boldsymbol{H}_{\mathrm{RT}} + \boldsymbol{H}_{\mathrm{TT}}, \quad (1)$$

where $\boldsymbol{H}_{\mathrm{v}}$, $\boldsymbol{H}_{\mathrm{R}}$, and $\boldsymbol{H}_{\mathrm{T}}$ describe the vibrational, overall rotational, and torsional motion, respectively. The term $\boldsymbol{H}_{\mathrm{RT}}$ accounts for coupling between the internal and overall rotation, while $\boldsymbol{H}_{\mathrm{TT}}$ represents couplings among different torsional states.

In the present treatment, the vibrational contribution enters only as an additive term to the total energy and does not mix with the rotational or torsional motion. Accordingly, $\boldsymbol{H}_{\mathrm{v}}$ is replaced by its eigenvalue E_{vib}. Neglecting all coupling terms, the resulting zeroth-order Hamiltonian is written as

$$\boldsymbol{H}_0 = E_{\mathrm{vib}} + \sum_{i=a,b,c} B_i \boldsymbol{J}_i^2 + F \boldsymbol{J}_\alpha^2 + V(\alpha), \quad (2)$$

where B_i ($i = a, b, c$) are the rotational constants defined as

$$B_i = \frac{h^2}{8\pi^2 I_i}, \quad (3)$$

of the asymmetric rotor associated with the components $\boldsymbol{J}_i$ of the total angular momentum operator along the principal inertial axes.

The constant F denotes the reduced internal rotation constant within the Combined Axis Method and accounts for the coupling between the internal rotor and the overall molecular rotation. It is related to the moment of inertia of the methyl top I_α and depends explicitly on the molecular inertia tensor through the geometric factor r,

$$F = \frac{h^2}{8\pi^2 r I_\alpha}, \tag{4}$$

where

$$r = 1 - \sum_{i=a,b,c} \frac{\lambda_i^2 I_\alpha}{I_i}. \tag{5}$$

Here, λ_i (i = a, b, c) are the direction cosines of the internal-rotation axis of the methyl top with respect to the principal inertial axes, *i.e.* the components of the unit vector $\mathbf{e}_\alpha = (\lambda_a, \lambda_b, \lambda_c)$. Since F depends on the rotational constants B_i through r, it varies slightly between different vibrational states. For practical reasons, and to separate purely torsional properties from vibrationally induced changes in the molecular geometry, it is therefore convenient to introduce the internal rotation constant

$$F_0 = \frac{h^2}{8\pi^2 I_\alpha}, \tag{6}$$

which depends only on the moment of inertia of the internal rotor. Within this formulation, the reduced internal rotation constant F entering the CAM Hamiltonian is obtained from the unreduced constant F_0 *via* the geometric correction factor r,

$$F = \frac{F_0}{r}. \tag{7}$$

For the CH_3 top, the internal rotation potential $V(\alpha)$ is expanded as a Fourier series in the torsional angle α,

$$V(\alpha) = \frac{V_3}{2}(1 - \cos 3\alpha) + \frac{V_6}{2}(1 - \cos 6\alpha) + \frac{V_9}{2}(1 - \cos 9\alpha) + \ldots, \tag{8}$$

where V_n (n = 3, 6, 9,...) denote the n-fold torsional barrier parameters.

Within the CAM framework, the torsional Hamiltonian $\boldsymbol{H}_T$ is formulated in the ρ-axis system (RAS). The corresponding matrix elements are expressed as

$$\langle \sigma K m | \boldsymbol{H}_T | \sigma K m \rangle = (3m - \rho K + \sigma)^2 F + \frac{1}{2}(V_3 + V_6 + V_9 + \ldots), \tag{9}$$

$$\langle \sigma K m | \boldsymbol{H}_T | \sigma K m \pm q \rangle = -\frac{1}{4} V_{3q}, \tag{10}$$

where m is the torsional quantum number, ρ is a dimensionless vector describing the projection of the internal rotor angular momentum onto the principal inertial axes, and K denotes the projection quantum number of the total angular momentum onto the principal axis. The torsional symmetry is labelled by σ (σ = 0 for A symmetry, σ = ±1 for E symmetry), and q is an integer describing the off-diagonality of the matrix element.

The torsional Hamiltonian matrix is diagonalised for K = $-J_{max}, \ldots, J_{max}$, yielding torsional energies $E^{RAS}_{T,K}$, which are subsequently transformed into the principal axis system (PAS) using Wigner D matrices.[16,19,26,27] The coupling terms $\boldsymbol{H}_{RT}$ and $\boldsymbol{H}_{TT}$ are negligible in the ground torsional state under the high-barrier approximation.[28] For torsionally excited states or lower barriers, their effects are accounted for in the GFC formalism by effective centrifugal distortion parameters such as D_J^E, D_K^E, D_-^E ..., and higher order parameters applied to the E-symmetry states, where n is the order of the respective operator. The matrix elements diagonal in the quantum number K are given by

$$\langle JK | D^E_{J^n} | JK \rangle = D^E_{J^n} J^n (J+1)^n \tag{11}$$

$$\langle JK | D^E_{K^n} | JK \rangle = D^E_{K^n} K^n \tag{12}$$

$$\langle JK | D^E_{J^n K^n} | JK \rangle = D^E_{J^n K^n} J^n (J+1)^n K^n \tag{13}$$

whereas the off-diagonal elements (ΔK = ±2) are expressed as:

$$\langle JK | D^E_- | JK \pm 2 \rangle = D^E_- \sqrt{[(J+1) - K(K \pm 1)][(J+1) - (K \pm 1)(K \pm 2)]} \tag{14}$$

$$\langle JK | D^E_{J_-} | JK \pm 2 \rangle = D^E_{J_-} J(J+1) \sqrt{[(J+1) - K(K \pm 1)][(J+1) - (K \pm 1)(K \pm 2)]} \tag{15}$$

$$\langle JK | D^E_{K^n -} | JK \pm 2 \rangle = D^E_{K^n -} K^n \sqrt{[(J+1) - K(K \pm 1)][(J+1) - (K \pm 1)(K \pm 2)]} \tag{16}$$

4 Quantum-chemical calculations

Quantum-chemical calculations were performed to support the analysis of the ro-vibrational spectrum of propylene oxide and to guide the assignment of the experimentally observed transitions. Equilibrium geometries and anharmonic vibrational frequencies were obtained using the Gaussian 16 program package,[29] employing second-order Møller–Plesset perturbation theory (MP2)[30] in combination with Dunning's correlation-consistent valence-polarized triple-ζ basis set augmented by diffuse functions (aug-cc-pVTZ).[31]

The calculated normal-mode displacement vectors of the ν_{17} = 1 vibrational mode are illustrated in Fig. 1. Based on the optimized geometry, approximate equilibrium rotational constants of A = 18 040 MHz, B = 6731 MHz, and C = 5986 MHz were obtained and used as initial values for the spectral assignments. The vibrational dependence of the rotational constants

was estimated using first-order vibration–rotation interaction constants α_i, according to

$$B_i = B_e - \sum_i \alpha_i \left(\nu_i + \frac{1}{2}\right), \quad (17)$$

where B_i and B_e denote the rotational constants in the ith vibrationally excited state and at the equilibrium geometry, respectively, and ν_i are the corresponding vibrational quantum numbers.

The anharmonic vibrational energy of the ν_{17} mode was calculated to be approximately 1022 cm^{-1}. In addition, the calculated transition dipole moment derivatives with respect to the normal coordinate Q, $\partial\mu/\partial Q_x = -5.6 \times 10^{-1}$ $(km\ mol^{-1})^{1/2}$, $\partial\mu/\partial Q_y = 2.6$ $(km\ mol^{-1})^{1/2}$, and $\partial\mu/\partial Q_z = 1.1$ $(km\ mol^{-1})^{1/2}$, indicate that the ν_{17} band exhibits predominantly b-type character, accompanied by weaker c-type and very weak a-type transitions.

5 Spectral analysis

5.1 Ground torsional state $\nu_T = 0$ and first torsionally excited state $\nu_{24} = 1$

The rotational spectrum of the ground torsional state $\nu_T = 0$ of propylene oxide has been extensively investigated in the microwave, millimetre- and submillimetre-wave region by Herschbach & Swalen[7,8] and more recently by Mesko *et al.*[10] The latter study reported 8514 *A* and 6686 *E* symmetry transitions. In the present work, this data set was curated and reanalysed using GFC. Transitions affected by unresolved *A*/*E* blends or distorted line shapes were removed, yielding 8048 *A* and 6573 *E* symmetry transitions (Table 1). The resulting fit reproduces the experimental frequencies with an RMS deviation of 80.6 kHz, a substantial improvement over the 191.5 kHz obtained in ref. 10.

Because the *A*/*E* splittings in the ground torsional state are only of the order of 1–2 MHz, the fit is only weakly sensitive to the parameters governing the torsional motion. In particular, the internal rotation constant F_0 and the threefold barrier height V_3 affect the splittings in a very similar manner and remain strongly correlated in a fit restricted to the ground state. This is reflected in a correlation coefficient of 0.97 between F_0 and V_3, indicating that these parameters cannot be determined independently from $\nu_T = 0$ data alone. Consequently, F_0 was kept fixed in the ground-state analysis.

Stahl *et al.*[11] analysed the first torsionally excited state $\nu_{24} = 1$ using 2526 *A* and 2452 *E* symmetry rotational transitions recorded between 75 and 950 GHz. In this state, the *A*/*E* splittings are much larger (up to 100 MHz) and exhibit a pronounced dependence on *J* and *K*, providing substantially increased sensitivity to the torsional parameters compared to the ground state. Nevertheless, a fit restricted to $\nu_{24} = 1$ still shows a strong correlation between F_0 and V_3. The corresponding

Table 1 Molecular parameters for the ground vibrational state and the first torsional state ($\nu_{24} = 1$) of propylene oxide, derived from curated linelists.[a] 1σ uncertainties are given in parentheses

	Separate fits				Simultaneous fit (this work)[b]	
Parameter	G.S. (ref. 10)	G.S. (this work)	$\nu_{24} = 1$ (ref. 11)	$\nu_{24} = 1$ (this work)[b]	G.S.	$\nu_{24} = 1$
A/MHz	18023.84513 (17)	18023.845657 (72)	18014.52748 (61)	18014.63073 (56)	18023.845687 (51)	18014.62408 (19)
B/MHz	6682.36952 (37)	6682.149511 (27)	6670.81061 (21)	6670.116888 (43)	6682.149516 (10)	6670.116691 (33)
C/MHz	5951.17621 (37)	5951.397142 (27)	5944.30048 (21)	5944.994967 (48)	5951.397151 (11)	5944.994745 (40)
Δ_J/kHz	2.914620 (41)	2.914841 (14)	2.89988 (14)	2.900014 (33)	2.914844 (10)	2.899855 (26)
Δ_{JK}/kHz	3.46722 (17)	3.466873 (56)	3.5932 (11)	3.53596 (22)	3.466892 (56)	3.53559 (19)
Δ_K/kHz	19.72715 (31)	19.729717 (96)	19.4579 (15)	19.8185 (21)	19.72970 (10)	19.79469 (89)
δ_J/kHz	0.192910 (13)	0.1927741 (14)	0.188471 (20)	0.1883670 (49)	0.1927741 (16)	0.1883715 (41)
δ_K/kHz	2.60044 (42)	2.597701 (99)	1.3474 (11)	2.18958 (33)	2.59767 (11)	2.18968 (28)
Φ_J/mHz	1.5343 (60)	1.5579 (20)	1.482 (33)	1.5875 (78)	1.5582 (19)	1.5557 (63)
Φ_{JK}/mHz	−6.72 (27)	−6.910 (12)	−14.39 (40)	−10.64 (10)	−6.908 (13)	−10.949 (83)
Φ_{KJ}/mHz	27.88 (90)	28.251 (33)	57.5 (15)	39.68 (34)	28.258 (35)	39.59 (29)
Φ_K/mHz	36.05 (65)	37.365 (46)	[0.0]	234.7 (19)	37.348 (50)	213.69 (91)
ϕ_J/mHz	0.0873 (24)	[0.083][c]	[0.0]	[0.083][c]	[0.083][c]	[0.083][c]
ϕ_{JK}/mHz	[0.0]	[−0.18][c]	[0.0]	[−0.18][c]	[−0.18][c]	[−0.18][c]
ϕ_K/Hz	0.1338 (58)	[0.13][c]	[0.0]	[0.13][c]	[0.13][c]	[0.13][c]
$\Delta_{\pi^2 J}$/MHz[d]	[0.0]	—	0.0488 (34)	—	—	—
$\Delta_{\pi^2 K}$/MHz[d]	−7.25 (11)	—	−0.391 (11)	—	—	—
F_0/GHz	[158.2278]	[159.86][e]	159.01 (16)	[159.86]	159.8600 (59)	
V_3/cm^{-1}	892.71 (58)	896.82 (20)	898.661 (89)	900.217 (12)	902.121 (87)	
V_6/cm^{-1}	—	—	—	—	−5.44 (25)	
δ/rad	0.4858 (19)	0.45896 (94)	0.4666 (12)	0.455829 (61)	0.456528 (34)	
ε/rad	1.55 (12)	[1.55][f]	1.574 (80)	[1.57][g]	[1.55][f]	
J_{max}/K_{max}	82/42	82/42	55/26	55/26	82/42	55/26
N^A/N^E[h]	8514/6686	8048/6573	2526/2452	2497/2414	8048/6573	2497/2414
RMS[i]/kHz	191.5	80.6	148.9	52.2	74.6	

[a] The refinement of linelists is described in Section 5.1. [b] The effective centrifugal distortion parameters determined in the analysis are given in Table 2. [c] Fixed at the calculated value (MP2/aug-cc-pVTZ). [d] $\Delta_{\pi^2 J}$ and $\Delta_{\pi^2 K}$ are empirical internal rotation–overall rotation distortion operators used in CAM/XIAM-type analyses.[11,32] [e] V_3, V_6, F_0, δ, and ε were determined in the simultaneous analysis of $\nu_T = 0$ and $\nu_{24} = 1$. [f] Fixed at the value reported by Mesko *et al.*[10] [g] Fixed at the value reported by Stahl *et al.*[11] [h] N^A/N^E correspond to the number of transitions of *A*- and *E*-symmetry. [i] RMS is the standard deviation of the fit.

Table 2 Effective centrifugal distortion parameters determined in the separate fit of transition frequencies of ν_{24} = 1 and in the simultaneous analysis of the ground torsional state and ν_{24} = 1

Parameter	Separate fit	Simultaneous fit
D_J^E/kHz	−0.603 (29)	−0.590 (24)
$D_{K^2}^E$/kHz	−163.26 (83)	−153.99 (36)
$D_{K^4}^E$/kHz	0.4552 (30)	0.4207 (13)
$D_{K^6}^E$/Hz	−0.3058 (27)	−0.2752 (13)
D_-^E/kHz	−0.9316 (76)	−0.9385 (67)
$D_{K^2-}^E$/Hz	7.26 (23)	7.69 (20)
$D_{K^4-}^E$/Hz	−43.90 (80)	−46.96 (69)
$D_{K^1}^E$/MHz	−0.9568 (45)	−0.9095 (23)
$D_{K^3}^E$/kHz	6.089 (42)	5.635 (20)
$D_{K^5}^E$/Hz	−9.418 (95)	−8.445 (53)
$D_{K^7}^E$/MHz	4.049 (68)	3.432 (44)
$D_{JK^1}^E$/Hz	48.70 (81)	52.82 (66)

Numbers in parentheses are the 1σ uncertainties.

correlation coefficient of 0.94 demonstrates that, despite the large splittings, the information content of a single torsional manifold is insufficient to fully disentangle these two parameters. Therefore, a curated line list of 2497 transitions of *A*-symmetry and 2414 transitions of *E*-symmetry was reanalysed using the improved ground-state constants shown in Table 2. The new set of parameters reduces the RMS value from 148.9 kHz to 52.2 kHz (Table 1). The resulting parameter set gives a consistent description of the torsional splitting and the associated centrifugal distortion effects.

A decisive reduction of the mutual correlation between F_0 and V_3 is achieved only when the refined ν_T = 0 and ν_{24} = 1 data sets are combined in a simultaneous GFC analysis. By exploiting the fundamentally different magnitudes and *J*, *K* dependences of the *A*/*E* splittings in the two torsional states, the parameter space is constrained from complementary directions. As a result, the correlation coefficient between F_0 and V_3 is reduced to 0.30 in the simultaneous fit, effectively breaking the near-linear dependence observed in the single-state analyses and allowing both parameters to be determined independently with high confidence.

In the separate fit of the ground state and the ν_{24} state we fixed F_0 to the value obtained from the simultaneous fit, which is F_0 = 159.86 GHz. The combined approach also enables a reliable determination of the small sixfold contribution V_6, which cannot be constrained from one torsional state alone. The parameters δ and ε describe the orientation of the internal rotor axis with respect to the principal axis system and the phase of the torsion–rotation interaction term in the effective Hamiltonian. In the simultaneous fit, ε shows strong correlations with other torsion–rotation parameters and could not be determined independently. It was therefore fixed to the value obtained from the ground-state analysis in the paper of Mesko *et al.*[10] The sextic centrifugal distortion parameters ϕ_J, ϕ_{JK}, and ϕ_K are only weakly constrained by the present dataset and were fixed to calculated values to stabilize the fit. The final torsional parameters from the simultaneous fit are listed in Table 1.

5.2 Vibrational mode ν_{17} = 1

The band origin of the ν_{17} fundamental, located at approximately 1023.5 cm^{-1}, was largely covered by the room-temperature measurements and exhibits a predominantly b-type band structure, in agreement with the *ab initio* predictions. Initial assignments were based on several unresolved Q-branches (K'' = 7–14, Fig. 2), as well as selected P-branch transitions (K'' = 0, and K'' = 7–9). In the vicinity of the band origin, several weak spectral features were observed that cannot be attributed to b-type transitions. The positions of these weak lines are in reasonable agreement with the expected locations of a- and c-type transitions inferred from the assigned b-type structure. However, due to their low intensity, these features could not be assigned unambiguously, and no quantitative conclusions regarding the relative transition dipole strengths could be drawn from the experimental data. The absence of reliably assignable a- and c-type transitions is consistent with their predicted weak intensities. The assignments were guided by spectral simulations employing the ground-state spectroscopic parameters listed in Table 1 together with the calculated band origin and vibration–rotation interaction constants. The resulting molecular constants were subsequently used to extend the assignments to spectra recorded under supersonic expansion conditions.

In the jet-cooled spectrum, all assigned b-type transitions in the R-, Q-, and P-branches with K'' = 0–4 form well-defined doublets (Fig. 3). The large splittings observed in the ν_{17} = 1 band (10–110 MHz) are far greater than the intrinsic torsional splitting expected for this vibrational mode (of order 1 MHz) and therefore indicate perturbative mixing with a nearby torsionally excited dark state. *Ab initio* calculations place several combination levels within a few cm^{-1} of ν_{17} (Fig. 1), and the

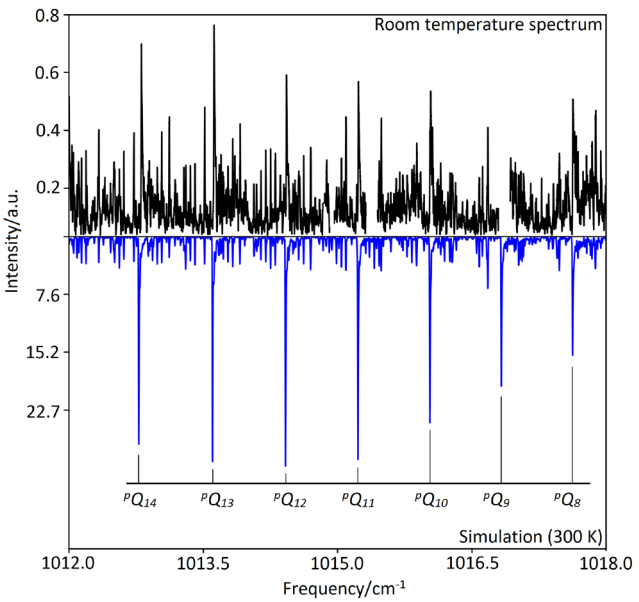

Fig. 2 Part of the measured (upper) and simulated (lower) P-branch transitions of propylene oxide. The strongest features correspond to unresolved Q-branches. The missing regions around 1015 and 1016.5 cm^{-1} are due to the mode hops of the QCL.

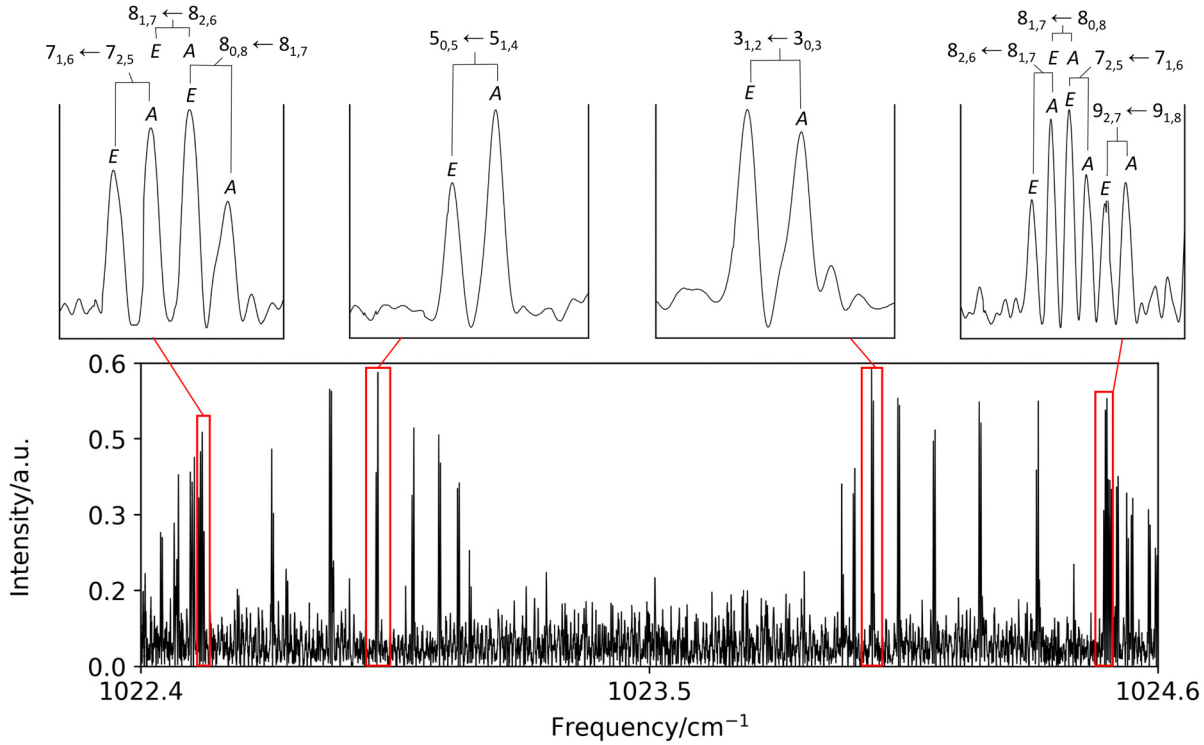

Fig. 3 Jet spectrum showing the band origin of ν_{17} = 1, with several zoomed-in views highlighting the resolved internal rotation splitting.

most plausible candidates involve an odd number of torsional quanta, *e.g.* combinations containing ν_{24} = 1, 3, or 5. For torsional manifolds of propylene oxide, the *A*/*E* level ordering alternates with the torsional quantum number; in particular, the experimentally established ordering in ν_{24} = 1 is *E* below *A*. Assuming that the dominant perturber carries an odd number of torsional quanta, the resolved ν_{17} doublets for $K_a'' = 0 - 4$ are therefore naturally assigned with the *E*-symmetry component at lower frequency and the *A*-dominated component at higher frequency.

This assignment is supported quantitatively by upper-state *A*/*E* offsets $\Delta E_u = E_u(E) - E_u(A)$ extracted from paired *A*- and *E*-symmetry transitions using combination differences (with the small ground-state *A*/*E* splitting accounted for). The mean offsets, averaged over all available K_c and $J \leq 15$, decrease systematically with increasing K_a for $K_a \leq 4$ (Fig. 5), *i.e.* the effective *A*/*E* splitting becomes progressively smaller at higher K_a.

At higher K_a the same trend manifests as a characteristic lineshape evolution. For $K_a'' = 5-7$, both the asymmetry splitting and the effective *A*/*E* splitting decrease to values comparable to the Doppler-limited linewidth (FWHM $\approx$ 40–50 MHz), and the components are no longer fully resolved (see Fig. 4). Instead, the transitions develop a reproducible low-frequency shoulder. The shoulder intensity is typically about one third of the main feature, consistent with an isolated *E*-symmetry contribution on the low-frequency side, whereas the high-frequency feature is dominated by an unresolved superposition in which two nearly coincident *A*-symmetry components overlap with an *E* contribution. The persistent appearance of the weaker feature at lower frequency thus supports an *E*-below-*A* ordering throughout the perturbed ν_{17} = 1 manifold.

The ν_{17} data were fitted in an effective Hamiltonian framework that captures the influence of the torsional dark state *via* symmetry-dependent term values and a small torsional correction. Accordingly, the observed level energies assigned to ν_{17} = 1 are written as

$$E_{obs} = E_{vib}^{A/E} + E_{rot} + E_{corr}, \quad (18)$$

with

$$E_{corr} = E_{vib+rot}^{\tau} - E_{vib}^{\tau}, \quad (19)$$

where τ denotes the torsional character of the perturbing contribution. The quantities E_{vib}^{A} and E_{vib}^{E} in Table 3 thus represent effective, symmetry-dependent band origins induced by the perturbation (not an intrinsic *A*/*E* splitting of the pure ν_{17} vibration). The rotational contribution E_{rot} is described by the rotational and centrifugal distortion constants, while the residual, rotation-dependent part of the splitting is captured through the effective torsional parameters (V_3, F_0, δ, ε), which should be regarded as phenomenological descriptors of rovibrational–torsional mixing. A simultaneous fit of the ground state and the ν_{17} state was tested but did not improve the stability of the fit due to strong parameter correlations arising from perturbative interactions with nearby torsional states. The ground-state constants were therefore fixed in the fit.

Using the resulting effective constants, additional b-type transitions in the room-temperature spectra were assigned,

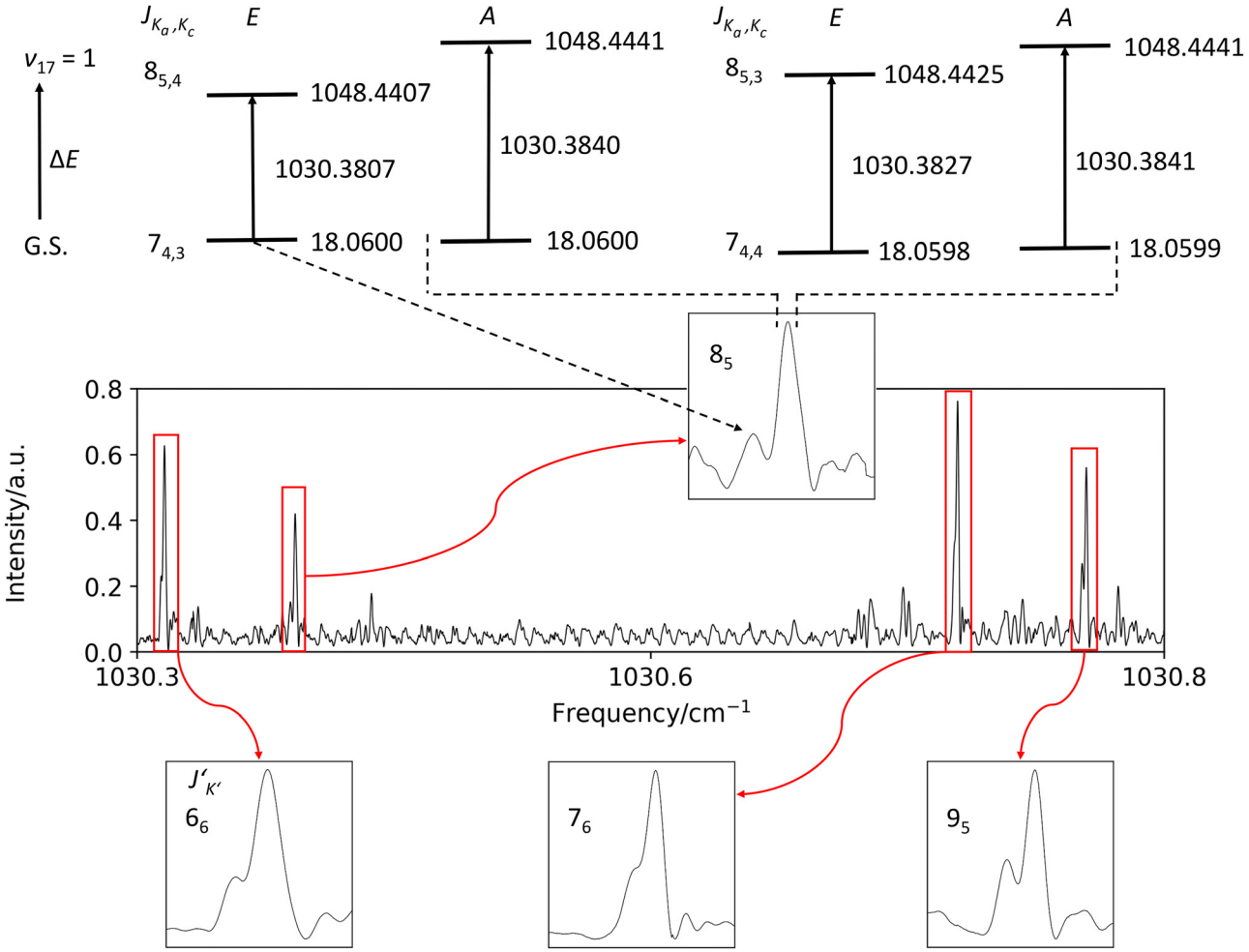

Fig. 4 Portion of the jet-cooled spectrum showing partially resolved *A*/*E* splittings in selected b-type R-branch transitions and the associated *K*-doubling of the *E*-symmetry species (four line pairs highlighted). The upper trace schematically illustrates the corresponding energy levels (in cm^{-1}). For the transition $J' = 8$, $K'_a = 5$, the lower-frequency component corresponds to the isolated $E(8_{5,4})$ line, while the higher-frequency feature arises from an unresolved overlap of $A(8_{5,4})$, $A(8_{5,3})$, and an *E* contribution. The splitting between $E(8_{5,4})$ and $E(8_{5,3})$ reflects *K*-doubling, *i.e.* the lifting of the $\pm K$ degeneracy in the *E* species. Because $E(8_{5,3})$ lies close to the *A* components, it is not fully resolved, resulting in an effective intensity ratio of approximately 1 : 3.

extending the data set to P- and R-branch lines with $K'' = 0$–10. Several Q-branch transitions with $K'' > 12$ could also be identified, but were excluded from the final fit because of pronounced systematic deviations from the predicted frequencies, indicative of interaction with a nearby vibrational state. The final analysis of the curated data set yielded the effective parameters summarized in Table 3; the complete line list is provided in the SI.

6 Results and discussion

The ground-state and first torsionally excited rotational spectra of propylene oxide were reanalysed using the General Fitting Code (GFC) and refined line lists. The improved data sets led to a substantial reduction of the RMS deviations and to significantly increased precision of the spectroscopic parameters compared to previous studies. A simultaneous treatment of both torsional states enabled an independent determination of the internal rotation constant F_0 and the threefold barrier height V_3, and allowed the sixfold torsional barrier term V_6 to be determined reliably.

The infrared spectrum of the $\nu_{17} = 1$ band exhibits systematic *A*/*E* splittings that cannot be attributed to intrinsic torsional splitting of this vibrational mode. Instead, the magnitude and ordering of the observed doublets indicate perturbative coupling with torsionally excited dark states. The consistent observation of the *E*-symmetry component at lower frequency across all assigned transitions provides strong evidence that the dominant interaction involves combination/overtone levels with an odd number of torsional quanta ν_{24}. Despite these perturbations, rotational series up to $J = 47$ and $K_a = 13$ could be assigned and analysed using an effective semi-rigid rotor Hamiltonian.

Guided by the vibrational energy level scheme shown in Fig. 1, several torsionally excited combination states emerge as

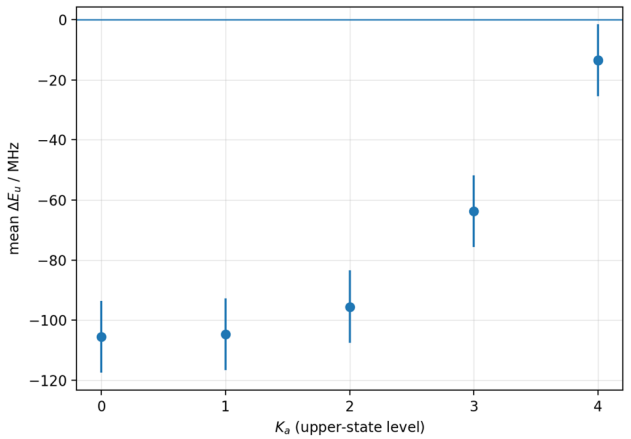

Fig. 5 Mean upper-state A/E offsets in the ν_{17} = 1 band as a function of K_a for $K_a \leq 4$. Offsets were obtained from paired A- and E-symmetry transitions using combination differences, yielding $\Delta E_u = E_u(E) - E_u(A)$ for individual upper-state levels. For each K_a, values were averaged over all available K_c and $J \leq 15$; points with $|\Delta E_u| < 6$ MHz were discarded. Error bars indicate the standard error of the mean (SEM). Negative offsets correspond to the observed E-below-A ordering.

Table 3 Effective spectroscopic parameters derived from the analysis of the perturbed ν_{17} = 1 band of propylene oxide

Parameter	ν_{17} = 1
E^A_{vib}/cm^{-1}	1023.517190 (39)
E^E_{vib}/cm^{-1}	1023.513785 (39)
A/MHz	18007.679 (67)
B/MHz	6677.721 (30)
C/MHz	5952.844 (15)
Δ_J/kHz	2.818 (12)
Δ_{JK}/kHz	−3.43 (26)
Δ_K/kHz	147.2 (11)
δ_J/kHz	0.1165 (88)
δ_K/kHz	[2.5977]
Φ_J/mHz	[1.5582]
Φ_{JK}/mHz	[−6.864]
Φ_{KJ}/mHz	[28.11]
Φ_K/mHz	[37.45]
ϕ_J/mHz	[0.083]
ϕ_{JK}/mHz	[−0.18]
ϕ_K/mHz	[130]
F_0/GHz	[159.86]
V_3/cm^{-1}	1102 (12)
δ/rad	[0.456516]
ε/rad	[1.55]
J_{max}/K_{max}	47/13
N^A/N^E	817/754
RMS/MHz	40.8

Numbers in parentheses give 1σ uncertainties in the last digit(s). E^A_{vib}, E^E_{vib} are the band origins of the A and E states respectively. Parameters in square brackets are fixed at ground state values. N^A/N^E correspond to number of A- and E symmetry transitions. RMS is the standard deviation of the fit.

plausible interaction partners. Based on *ab initio* estimates, these include $5\nu_{24}$ ($\approx$1020.0 cm^{-1}), $3\nu_{24} + \nu_{22}$ ($\approx$1019.6 cm^{-1}), and $\nu_{24} + 2\nu_{22}$ ($\approx$1018.0 cm^{-1}), all lying within a few wavenumbers of the ν_{17} fundamental at $\approx$1022.5 cm^{-1}. All proposed candidates contain an odd number of torsional quanta and are therefore symmetry-compatible with the observed E-below-A ordering. Given the limited accuracy of the calculated combination-level energies, particularly for multiply excited states, the energetic ordering of these candidates should not be over-interpreted. Thus, while the experimental data clearly point to a dominant torsional contribution, the dense manifold of nearby states and the approximate nature of the energies prevent a unique identification of the specific perturbing dark state.

Author contributions

K. Vávra: conceptualization, investigation, formal analysis, data curation, software, writing – original draft. K. Luková: data curation, formal analysis, writing – original draft. E. Döring: investigation, writing – original draft. J. Jakob: investigation, writing – review. T. F. Giesen and G. W. Fuchs: funding acquisition, supervision, writing – review and editing.

Conflicts of interest

There are no conflicts to declare.

Data availability

The data supporting this article, including lists of assigned transitions and output files from the fitting procedure, are provided in the supplementary information (SI). See DOI: https://doi.org/10.1039/d6cp00517a.

The General Fitting Code (GFC) program is publicly available *via* the Zenodo repository at https://doi.org/10.5281/zenodo.17287288.

Appendix

A Appendix

The General Fitting Code (GFC) is a newly developed versatile tool for the analysis of pure rotational, vibrational and rovibrational spectra. It is suitable for the analysis of asymmetric tops as well as species with a single internal rotor with C_{3v} symmetry. In this sense, GFC represents a new member of the family of programs developed for the analysis of internal rotation effects, complementing established tools such as XIAM,[19,21,33,34] BELGI,[20,21,27] ERHAM,[35–37] RAM36,[24,38,39] and Westerfit.[25] The program is written in the *Python* (https://www.Python.org) programming language, the majority of numerical calculations are performed in *Julia* (https://julialang.org/) to enhance the performance and speed of the computation routines.

The General Fitting Code (GFC) program is available in the Zenodo repository, see DOI: https://doi.org/10.5281/zenodo.17287288. Any questions concerning GFC should be addressed to Dr Karel Vávra (vavrak@vscht.cz).

The main features of the software involve:

- Visualisation of experimental spectra (ASCII format)

- Processing of spectra (smoothing, convolution functions, ...)
- Calculation and visualization of spectral predictions
- Loomis–Wood type plots, Fortrat diagrams, Reduced energy diagrams
- Line profile fitting, quantum numbers assignment
- Least square fitting (Gauss–Newton method) of parameters to Hamiltonian matrix elements
- Ro-vibrational coupling
- Plural nuclear quadrupole coupling
- Internal rotation (combined axis method, one C_{3v} internal rotor, no symmetry constraints for the molecular frame)
- No imposed limits on quantum numbers, number of transitions, or vibrational/torsional states.
- Partition function calculations
- Export of high-quality figures in .eps, .svg, .png formats

GFC is designed to accommodate a wide range of spectroscopic problems. It features a graphical user interface (GUI) for intuitive operation, enabling users to construct the Hamiltonian matrix using predefined matrix elements. These include *A*- and *S*-reduced effective rotational Hamiltonian in different representations, second-order ro-vibrational terms, nuclear quadrupole couplings, and internal rotation parameters. Users can also define custom-made matrix elements within a symmetric top basis set tailored to the molecular system under investigation.

The predefined matrix elements for constructing the full Hamiltonian are as follows

$$\boldsymbol{H} = \boldsymbol{H}_{\mathrm{R}} + \boldsymbol{H}_{\mathrm{CD}} + \boldsymbol{H}_{\mathrm{T}} + \boldsymbol{H}_{\mathrm{P}} + \boldsymbol{H}_{Q1} + \cdots + \boldsymbol{H}_{Qn} \tag{20}$$

and are further described in the following enumeration:

- Rotational Hamiltonian $\boldsymbol{H}_{\mathrm{R}}$ for an asymmetric top in any representation:

$$\langle JK|\boldsymbol{H}_{\mathrm{R}}|JK\rangle = \frac{1}{2}(B_x + B_y)J(J+1) + \left(B_z - \frac{B_x + B_y}{2}\right)K^2 \tag{21}$$

$$\langle JK|\boldsymbol{H}_{\mathrm{R}}|JK \pm 2\rangle = \frac{1}{4}(B_x - B_y)F(J,K)F(J,K\pm 1) \tag{22}$$

- Centrifugal distortion (CD) parameters diagonal in K:

$$\begin{aligned}\langle JK|\boldsymbol{H}_{\mathrm{CD}}|JK\rangle = {} & -\Delta_J J^2(J+1)^2 + \Phi_J J^3(J+1)^3 \\ & + L_J J^4(J+1)^4 + \cdots \\ & - \Delta_{JK} J(J+1)K^2 + \Phi_{JK} J^2(J+1)^2 K^2 \\ & + L_{JJK} J^3(J+1)^3 K^2 + \cdots \\ & + \Phi_{KJ} J(J+1)K^4 + \cdots + L_{KKJ} J(J+1)K^6 + \cdots \\ & - \Delta_K K^4 + \Phi_K K^6 + L_K K^8 + \text{higher order terms}\end{aligned} \tag{23}$$

- CD parameters off-diagonal in $K \pm 2$ (*A*-reduction):

$$\begin{aligned}\left\langle JK\left|\boldsymbol{H}_{\mathrm{CD}}^{(A)}\right|JK\pm 2\right\rangle = {} & \Big[\delta_J J(J+1) - \frac{1}{2}\delta_K\left[K^2 + (K\pm 2)^2\right] \\ & + \phi_J J^2(J+1)^2 + \frac{1}{2}\phi_{JK} J(J+1) \\ & \times \left[K^2 + (K\pm 2)^2\right] \\ & + \frac{1}{2}\phi_K\left[K^4 + (K\pm 2)^4\right] \\ & + \text{higher order terms}\Big] F(J,K)F(J,K\pm 1)\end{aligned} \tag{24}$$

- CD parameters off-diagonal in $K \pm 2n$, where n is an integer: $n = 1, 2, 3, \ldots$ (*S*-reduction):

$$\begin{aligned}&\left\langle JK\left|\boldsymbol{H}_{\mathrm{CD}}^{(S)}\right|JK\pm 2n\right\rangle \\ &= \left[d_1 J(J+1) + h_1 J^2(J+1)^2 + l_1 J^3(J+1)^3\right. \\ &\quad \left. + p_1 J^4(J+1)^4 + \text{higher order terms}\right] \\ &\quad \times F(J,K)F(J,K\pm 1); \\ &= \left[d_2 + h_2 J(J+1) + l_2 J^2(J+1)^2 + p_2 J^3(J+1)^3\right. \\ &\quad \left. + \text{higher order terms}\right] F(J,K)F(J,K\pm 1) \\ &\quad \times F(J,K\pm 2)F(J,K\pm 3); \\ &= \left[h_3 + l_3 J(J+1) + p_3 J^2(J+1)^2 + \text{higher order terms}\right] \\ &\quad \times F(J,K)F(J,K\pm 1)F(J,K\pm 2)F(J,K\pm 3) \\ &\quad \times F(J,K\pm 4)F(J,K\pm 5);\end{aligned} \tag{25}$$

- The matrix elements of the torsional Hamiltonian in the rho-axis system are given in eqn (9) and (10) in the main text. Additional effective parameters defined in eqn (11), (12) and (14) can be included in the semi-rigid rotor Hamiltonian for the *E*-symmetry state(s) to treat further perturbation arising from coupling between overall and internal rotation.
- First order a-type Coriolis mixing (G_{a}) matrix element:

$$\langle J,K,\nu_i|\boldsymbol{H}_{\mathrm{P}}|J,K,\nu_i'\rangle = \frac{i}{2}KG_{\mathrm{a}} \tag{26}$$

- Second order a-type Coriolis mixing (F_{bc}) matrix element:

$$\langle J,K,\nu_i|\boldsymbol{H}_{\mathrm{P}}|J,K\pm 2,\nu_i'\rangle = \mp\frac{i}{2}F_{\mathrm{bc}}[F(J,K)F(J,K\pm 1)] \tag{27}$$

- First order b-type Coriolis mixing (G_{b}) matrix element:

$$\langle J,K,\nu_i|\boldsymbol{H}_{\mathrm{P}}|J,K\pm 1,\nu_i'\rangle = \frac{i}{2}G_{\mathrm{b}}[F(J,K)] \tag{28}$$

- Second order b-type Coriolis mixing (F_{ac}) matrix element:

$$\langle J, K, \nu_i | \boldsymbol{H}_P | J, K \pm 1, \nu_i' \rangle = \mp \frac{i}{2} F_{ac}(2K \pm 1)[F(J,K)] \quad (29)$$

- First order c-type Coriolis mixing (G_c) matrix element:

$$\langle J, K, \nu_i | \boldsymbol{H}_P | J, K \pm 1, \nu_i' \rangle = \pm \frac{1}{2} G_c[F(J,K)]F(J,K) \quad (30)$$

- Second order c-type Coriolis mixing (F_{ab}) matrix element:

$$\langle J, K, \nu_i | \boldsymbol{H}_P | J, K \pm 1, \nu_i' \rangle = \frac{1}{2} F_{ab}(2K \pm 1)[F(J,K)] \quad (31)$$

- Matrix elements for Fermi resonance/anharmonic (W) coupling:

$$\langle J, K, \nu_i | \boldsymbol{H}_P | J, K, \nu_i' \rangle = W \quad (32)$$

$$\langle J, K, \nu_i | \boldsymbol{H}_P | J, K \pm 2, \nu_i' \rangle = W^{\pm}[F(J,K)F(J,K \pm 1)] \quad (33)$$

$$F(J,K) = \sqrt{J(J+1) - K(K \pm 1)} \quad (34)$$

- Matrix elements, including those off-diagonal in J and K, of the quadrupole interaction Hamiltonian for one nucleus:[40]

$$\langle J, K, F_1 | \boldsymbol{H}_{Q1} | J', K', F_1 \rangle = \chi_n (-1)^{t_1} [(2J+1)(2J'+1)]^{1/2} \times \begin{Bmatrix} F_1 & I_1 & J \\ 2 & J' & I_1 \end{Bmatrix} \begin{pmatrix} J & 2 & J' \\ -K & -q & K' \end{pmatrix} \times \begin{pmatrix} I_1 & 2 & I_1 \\ -I_1 & 0 & I_1 \end{pmatrix}^{-1} \quad (35)$$

$$t_1 = J + J' + K + F_1 + I_1 \quad (36)$$

where I is the spin quantum number, F is the total angular momentum quantum number $F = J + I$ and q is an integer $q = K - K'$

- Matrix elements for n nuclei, including those off-diagonal in J, K, and $F_1, \ldots, F_{n-1}$, of the quadrupole interaction Hamiltonian:[41]

$$\langle J, K, F_1, F_2, \ldots, F | \boldsymbol{H}_{Qn} | J', K', F_1', F_2', \ldots, F \rangle = \chi_n (-1)^{t_n} [(2J+1)(2J'+1)]^{1/2} \times \left[(2F_1+1)(2F_1'+1)\right]^{1/2} \ldots \left[(2F_{n-1}+1)(2F_{n-1}'+1)\right]^{1/2} \times \begin{Bmatrix} J' & F_1' & I_1 \\ F_1 & J & 2 \end{Bmatrix} \begin{Bmatrix} F_1' & F_2' & I_2 \\ F_2 & F_1 & 2 \end{Bmatrix} \ldots \begin{Bmatrix} F_n & I_n & F_{n-1} \\ 2 & F_{n-1}' & I_n \end{Bmatrix} \times \begin{pmatrix} J & 2 & J' \\ -K & -q & K' \end{pmatrix} \begin{pmatrix} I_n & 2 & I_n \\ -I_n & 0 & I_n \end{pmatrix}^{-1} \quad (37)$$

$$t_n = J + K + \sum_{i=1}^{n-1} (F_{i-1}' + I_i + F_i) + (F_{n-1} + I_n + F_n) \quad (38)$$

$$q = K' - K \quad (39)$$

χ_n:

$$\chi_0 = \frac{\chi_{zz}}{4} \quad (40)$$

$$\chi_{\pm 1} = \mp \left(\frac{2}{3}\right)^{1/2} \frac{(\chi_{xz} \pm i\chi_{yz})}{4} \quad (41)$$

$$\chi_{\pm 2} = \left(\frac{1}{6}\right)^{1/2} \frac{(\chi_{xx} - \chi_{yy} \pm 2i\chi_{xy})}{4} \quad (42)$$

where χ is the quadrupole coupling tensor $\chi_q = eQV_q$ with e as elemental charge, Q as nuclear electric quadrupole moment and V_q as electric field gradient. The terms enclosed in round and curly brackets in eqn (35) and (37) correspond to the Wigner 3j and 6j symbols.

The implementation of the rho-axis method to treat internal rotation, as well as the extension of the program applicability to two and more internal rotors and to symmetric and linear molecules, is currently in progress.

Acknowledgements

The authors thank P. Stahl for providing the experimental spectrum used in the analysis of the ground vibrational state and the first torsionally excited state in this study. The authors also thank Y. Kawashima and S. Herbers for discussions on the internal-rotation analysis and fitting-code development. This project was supported by the DFG *via* grant SFB 1319 ELCH and the DFG grant 466220934 (FU 715/4-1).

Notes and references

1 K. Vávra, E. Döring, J. Jakob, F. Peterß, M. Kaufmann, P. Stahl, T. F. Giesen and G. W. Fuchs, *Phys. Chem. Chem. Phys.*, 2024, **26**, 23886–23892.
2 V. Barone, M. Biczysko, J. Bloino and C. Puzzarini, *J. Chem. Phys.*, 2014, **141**, 034107.
3 S. Luber, M. Ianuzzi and J. Hutter, *J. Chem. Phys.*, 2014, **141**, 094503.
4 M. C. Tam, N. J. Russ and T. D. Crawford, *J. Chem. Phys.*, 2004, **121**, 3550–3557.
5 M. Hodecker, M. Biczysko, A. Dreuw and V. Barone, *J. Chem. Theory Comput.*, 2016, **12**, 2820–2833.
6 B. A. McGuire, P. B. Carroll, R. A. Loomis, I. A. Finneran, P. R. Jewell, A. J. Remijan and G. A. Blake, *Science*, 2016, **352**, 1449–1452.
7 J. D. Swalen and D. R. Herschbach, *J. Chem. Phys.*, 1957, **27**, 100–108.

8 D. R. Herschbach and J. D. Swalen, *J. Chem. Phys.*, 1958, **29**, 761–776.
9 W. Fateley and F. A. Miller, *Spectrochim. Acta*, 1963, **19**, 611–628.
10 A. Mesko, L. Zou, P. B. Carroll and S. L. Widicus Weaver, *J. Mol. Spectrosc.*, 2017, **335**, 49–53.
11 P. Stahl, B. E. Arenas, O. Zingsheim, M. Schnell, L. Margules, R. A. Motiyenko, G. W. Fuchs and T. F. Giesen, *J. Mol. Spectrosc.*, 2021, **378**, 111445.
12 F. X. Sunahori, Z. Su, C. Kang and Y. Xu, *Chem. Phys. Lett.*, 2010, **494**, 14–20.
13 A. Ainetschian, G. T. Fraser, J. Ortigoso and B. H. Pate, *J. Chem. Phys.*, 1994, **100**, 729–732.
14 W. J. Lafferty, J.-M. Flaud and M. Herman, *J. Mol. Struct.*, 2006, **780**, 65–69.
15 D. Witsch, E. Döring, A. A. Breier, J. Gauss, T. F. Giesen and G. W. Fuchs, *J. Phys. Chem. A*, 2023, **127**, 3824–3831.
16 R. C. Woods, *J. Mol. Spectrosc.*, 1966, **21**, 4–24.
17 J. K. G. Watson, *Vibrational Spectra and Structure*, 1977, pp. 1–89.
18 I. Kleiner, *J. Mol. Spectrosc.*, 2010, **260**, 1–18.
19 H. Hartwig and H. Dreizler, *Z. Naturforsch., A*, 1996, **51**, 923–932.
20 J. Hougen, I. Kleiner and M. Godefroid, *J. Mol. Spectrosc.*, 1994, **163**, 559–586.
21 S. Khemissi, S. Herbers, I. Gulaczyk, M. Kreglewski, P. Asselin, S. Chawananon, H. V. L. Nguyen and I. Kleiner, *J. Quant. Spectrosc. Radiat. Transfer*, 2025, **346**, 109601.
22 P. Groner, *J. Chem. Phys.*, 1997, **107**, 4483.
23 P. Groner, *J. Mol. Spectrosc.*, 2012, **278**, 52.
24 V. V. Ilyushin, Z. Kisiel, L. Pszczókowski, H. Mäder and J. T. Hougen, *J. Mol. Spectrosc.*, 2010, **259**, 26–38.
25 J. Westerfield and S. Worthington-Kirsch, *J. Mol. Spectrosc.*, 2024, **404**, 111928.
26 E. P. Wigner, *Gruppentheorie und ihre Anwendung auf die Quantenmechanik der Atomspektren*, Springer, 1944.
27 I. Kleiner and J. T. Hougen, *J. Chem. Phys.*, 2003, **119**, 5505–5509.
28 C. C. Lin and J. D. Swalen, *Rev. Mod. Phys.*, 1959, **31**, 841.
29 M. J. Frisch, G. W. Trucks, H. B. Schlegel, G. E. Scuseria, M. A. Robb, J. R. Cheeseman, G. Scalmani, V. Barone, G. A. Petersson, H. Nakatsuji, X. Li, M. Caricato, A. V. Marenich, J. Bloino, B. G. Janesko, R. Gomperts, B. Mennucci, H. P. Hratchian, J. V. Ortiz, A. F. Izmaylov, J. L. Sonnenberg, D. Williams-Young, F. Ding, F. Lipparini, F. Egidi, J. Goings, B. Peng, A. Petrone, T. Henderson, D. Ranasinghe, V. G. Zakrzewski, J. Gao, N. Rega, G. Zheng, W. Liang, M. Hada, M. Ehara, K. Toyota, R. Fukuda, J. Hasegawa, M. Ishida, T. Nakajima, Y. Honda, O. Kitao, H. Nakai, T. Vreven, K. Throssell, J. A. Montgomery, Jr., J. E. Peralta, F. Ogliaro, M. J. Bearpark, J. J. Heyd, E. N. Brothers, K. N. Kudin, V. N. Staroverov, T. A. Keith, R. Kobayashi, J. Normand, K. Raghavachari, A. P. Rendell, J. C. Burant, S. S. Iyengar, J. Tomasi, M. Cossi, J. M. Millam, M. Klene, C. Adamo, R. Cammi, J. W. Ochterski, R. L. Martin, K. Morokuma, O. Farkas, J. B. Foresman and D. J. Fox, *Gaussian16 Revision C.01*, Gaussian Inc., Wallingford CT, 2016.
30 M. J. Frisch, M. Head-Gordon and J. A. Pople, *Chem. Phys. Lett.*, 1990, **166**, 275–280.
31 R. A. Kendall, T. H. Dunning Jr and R. J. Harrison, *J. Chem. Phys.*, 1992, **96**, 6796–6806.
32 N. Hansen, H. Mäder and T. Bruhn, *Mol. Phys.*, 1999, **97**, 587–595.
33 S. Herbers and H. V. L. Nguyen, *J. Mol. Spectrosc.*, 2020, **370**, 111289.
34 S. Herbers, *J. Mol. Spectrosc.*, 2024, **405**, 111950.
35 P. Groner, S. Albert, E. Herbst and F. C. De Lucia, *Astrophys. J.*, 1998, **500**, 1059.
36 P. Groner, E. Herbst, F. C. De Lucia, B. J. Drouin and H. Mäder, *J. Mol. Struct.*, 2006, **795**, 173–178.
37 P. Groner, I. R. Medvedev, F. C. De Lucia and B. J. Drouin, *J. Mol. Spectrosc.*, 2008, **251**, 180–184.
38 V. V. Ilyushin, C. P. Endres, F. Lewen, S. Schlemmer and B. J. Drouin, *J. Mol. Spectrosc.*, 2013, **290**, 31–41.
39 V. Ilyushin, *J. Mol. Spectrosc.*, 2018, **345**, 64–69.
40 H. P. Benz, A. Bauder and H. H. Günthard, *J. Mol. Spectrosc.*, 1966, **21**, 156–164.
41 P. Thaddeus, L. C. Krisher and J. H. N. Loubser, *J. Chem. Phys.*, 1964, **40**, 257–273.

